Zhang Lihai (Orcid ID: 0000-0002-1282-992X)

Infrared thermography detection of delamination in bottom of concrete bridge decks

Babar Nasim Khan Raja, Saeed Miramini, Colin Duffield, Massoud Sofi, Lihai Zhang*
Department of Infrastructure Engineering, University of Melbourne, Victoria 3010, Australia

Correspondence:
Lihai Zhang
Department of Infrastructure Engineering, University of Melbourne, Victoria 3010, Australia
Email: lihzhang@unimelb.edu.au

Abstract

Infrared thermography (IRT) has been widely used in detecting the subsurface delamination of bridge deck. However, IRT inspection on delamination zones of the bridge deck which have limited exposure to direct solar radiation (*e.g.* the bottom surface of the bridge deck) is rather challenging due to the relatively low thermal contrast (ΔT) development in these zones. Therefore, the purpose of this study is to conduct a series of experimental studies in conjunction with numerical modelling for investigating the effectiveness of IRT in delamination detection of bridge deck components which are normally not exposed to direct solar radiation. Specially, the effects of different environmental conditions, thickness of bridge deck and defect characteristics on the absolute thermal contrast (ΔT) development were systematically investigated. The results show that IRT can effectively detect the subsurface delamination of concrete bridge deck located in regions that are not exposed to the direct solar radiation. In addition, the development of detectable thermal contrast (> 0.5°C) is much dependent on the rate of change in ambient temperature with a suitable detection period between 8am and 4pm. Furthermore, it shows that the value of ΔT increases with the increase of bridge deck thickness and delamination size.

Keywords: Infrared thermography (IRT); bridge deck; bridge soffit; delamination; thermal contrast; solar radiation; ambient temperature

1 INTRODUCTION

Concrete is a popular material for bridge construction, especially for the bridge decks. However, the concrete members in bridges can deteriorate as a result of aging, and environmental severity[1]. In addition, the abrasion and repeated heavy loading on the bridge deck lead to surface cracking and damages in the structure[2, 3]. Reinforcing bars (rebars) corrosion is the principal cause of reinforced concrete (RC) deterioration in the form of cover cracking, delamination, and spalling[4-6]. The formation of iron oxide around the rebars causes the expansion of steel, which imposes tensile stresses on concrete leading towards cracking and weakening of concrete bond with rebars[7, 8]. These cracks then propagate along with the rebar mesh, parallel to the concrete surface, ultimately yield the subsurface delamination in concrete. Without timely repairing, concreate cracking could lead to the spalling of the concrete chunk, resulting in a pothole on the surface; which further exposes the rebars to the environment and expedites the rate of deterioration[9]. Concrete delamination is not only limited to the concrete bridge deck but also the concrete soffits, girders, piers, and abutments of the bridge[10-13]. In the past, fatalities have been reported due to concrete spall falling onto a motorist from the soffit of an overpass bridge[11]. Concrete is the second most used material in the world

after water[14, 15]. The overall annual cost of repair and maintenance for corrosion-induced deterioration in RC structures is estimated to be around $100 billion, worldwide[16]. Therefore, the early-stage recognition and remedial measures of concrete delamination are necessary to avoid deterioration and uncontrolled spall and damages in bridge structures.

Current bridge inspection techniques primarily rely on visual inspections. However, subsurface damages are invisible to the human eye. Therefore, visual defect detection is rather challenging. To address this problem, several non-destructive techniques have been developed and applied in engineering practice. For example, visual inspection along with hammer sounding and coin tapping, chain dragging, Impact echo, electric resistivity, ultrasonic surface wave, ground penetration radar, and infrared thermography (IRT)/thermal imaging have been previously used for structural health monitoring of bridges[17-22]. IRT has the advantage of quickly scanning the 2D surface using an infrared camera, without affecting the bridge operation [23]. In addition, the remote scanning capability of IRT allows the inspection of bridge girders and lower surface of the bridge deck which are difficult to access during inspection. In the recent years unmanned arial vehicle (UAV) borne thermal imaging system has gained significant interest of researchers and considered as a valuable option to inspect inaccessible bridge areas[24-28]. The UAV sensors could conduct inspection in an efficient and cost-effective manner as well as minimizing the traffic disturbance and creating a safe working environment[28]. Although IRT has the capability of producing good results for the subsurface damage characterization, it has some drawbacks, such as lack of detailed information about the defect characteristics. In addition, the IRT measurement outcomes are very sensitive to environment conditions[29], and the surface texture of the concrete members[30].

Every object having a temperature above absolute zero radiates thermal energy in the long infrared range of the electromagnetic spectrum. For IRT inspection, the radiations from the concrete surface are firstly captured by thermal cameras, and then converted into temperature pixels on a thermogram. The variation in the surface temperature of concrete in a thermogram indicates the presence of anomalies within the concrete[31]. The principal of IRT is based on the concept that, due to low thermal conductivity, air filled gaps within concrete disrupt heat flow through the delaminated region and create a different radiant temperatures on the thermogram, as compared to that of the nearby intact concrete region[29]. However, the non-uniform temperature distribution within the concrete may cause some issues[32]. For example, the IRT results for the in-situ detection of defects could be affected by the solar radiation variations and shading caused by some surrounding objects etc. Similarly, the condition of the concrete surface under observation could also cause false detection of anomalies (e.g., texture and color variation and possible foreign object on the surface)[33].

There are two approaches for conducting Infrared thermography, *i.e.,* active thermography and passive thermography. Active thermography involves the heating of concrete members using non-natural heat sources and collecting data during heating or cooling phases, whereas the passive thermography uses energy from natural heat sources for heat exchange with the concrete, such as solar radiation and daily temperature variationstru[34, 35] .As active thermography is expensive to carry out for large engineering structures, the passive infrared thermography is commonly used for delamination detection of concrete structures, particularly

the concrete bridge decks. Direct sunlight, which transports the thermal energy from solar radiation into the surface of concrete and causes the concrete to heat up, is considered as a primary driving force for the thermal gradient development[31, 36]. ASTM D4788-03 is one of the commonly used guidelines for delamination detection in bridge deck using infrared thermography[37]. It describes the test method and feasible environmental conditions for conducting IRT in the field, and recognizes the importance of the direct sunlight for the success of IRT method.

The delamination underneath the deck, and soffit area of the bridges poses a serious threat to the vehicles passing below. However, as these bridge members usually do not experience direct sunlight, there are no clear guidelines available for detecting delamination underneath bridge decks and soffit areas using IRT so far, and relevant research in this field is limited[10, 11, 38]. Clark et.al [10] performed field inspection of the underside of bridge deck using IRT, and found that IRT is able to identify the delamination of concrete deck under relatively low ambient temperatures and without radiant heating from the sun. However, the environmental factor is still one of the critical factors that could highly affect the thermographic results. Washer et. al [11] conducted experiments on a big concrete block to study the application of IRT for delamination detection in shaded regions. Their results show that high daily variation in temperature is required to produce a measurable thermal gradient on the concrete surface, and the detectability of defects could be enhanced with the increase in the rate of change of ambient temperature. A recent experimental study on IRT measurement on members unexposed to sunlight[38] shows that defect detection is possible only for a short time period and the quantitative estimation of defect characteristics is not possible. However, the convection heat transfer because of daily temperature variation and indirect solar radiation impact has not been fully understood.

Sun is the major heat source for passive IRT. If the bridge members are subjected to the direct sunlight, the primary heat exchange takes place through the solar radiations. Previous studies mainly focused on IRT inspection of bridge deck exposed to direct sunlight (*i.e.,* the top surface of the deck)[2, 31, 34, 37, 39-42]. However, some bridge members are in shaded regions, and thereby not exposed to direct solar radiation. The relevant research in this field is limited. Therefore, the purpose of this study is to investigate the thermal response of subsurface defects in bottom concrete bridge deck, and thermal exchange between concrete and surrounding environment. Particularly, both experimental and numerical studies were carried out to investigate two IRT inspection cases as shown in Figure 1, *i.e.* Case-A: Not exposed to the solar radiations at all; and Case B: Exposed to indirect solar radiations impacts (i.e., the surface under observation does not face direct sunlight however, the back of the member is exposed to the solar radiations).

2 MATERIALS AND METHODS

2.1 Methodology

Figure 1 shows that the applicability of IRT for defect detection in concrete relies on the temperature difference between sound and delaminated areas (*i.e.* thermal contrast). First, a series of experimental studies were performed. Then, a numerical model was developed, and the numerical predictions were validated by the experimental data. Finally, the effects of defect

characteristics (e.g. size, depth, thickness) and different inspections time windows, which have significant impact on thermal contrast[17, 23, 36, 39-42], were also investigated by conducting a series of parametric studies.

2.2 Experimental study

2.2.1 Preparation of concrete slab samples

Two reinforced concrete slabs were prepared based on the design of normal concrete bridge deck (*i.e.* S-1 and S-2 shown in Figure 2). Polystyrene styrofoam were embedded into the slabs to mimic subsurface delamination in bridge deck. Since subsurface delamination is air filled gap within concrete, styrofoam is used to simulate the thermal behaviour of delamination in concrete due to its thermal conductivity (0.033 W/m.ºC), which is similar to that of air (0.0241W/m.ºC)[30]. The thickness of both slabs was taken as 175mm like the thickness of many bridge decks. Reinforcement bars (12mm in diameter, grade 500) were used in the sample construction which hold the styrofoam during slab casting and provide the tensile strength to the concrete as well. Three delamination types (*i.e.* D1, D2, and D3) were designed using styrofoam. The depth and size of delamination are chosen to simulate the influence of the defects with different sizes and depths in IRT measurement outcomes. The D1 has an area of 200 cm^2 with a depth of 63 mm from slab surface, while D2 and D3 has an area of 100 cm^2 each and located at 63 and 38 mm from the surface, respectively. In this way, the defects with the combination of two different sizes and two different depths could be experimentally investigated. The details of the slab samples are shown in Table 1 and Table 2, respectively. After setting of concrete, the four sides of slabs were insulated using extruded polystyrene boards to imitate a large concrete bridge deck by minimizing the heat exchange through the sides of concrete samples.

2.2.2 Experimental procedure

The experiments were set up in natural environmental conditions at University of Melbourne, Australia. To collect the real time weather data a local weather station (Digitech Wireless Weather Station XC0348) was setup beside the concrete slabs. Solar radiation (W/m^2) on the concrete surface were measured using radiation flux sensor (TRFS 50x50) by Captec enterprise®, attached on the back of concrete slab (S-1). Two thermocouples were also installed at the surface of radiant flux sensor and concrete surface, respectively, to measure the surface temperatures. Graphtec GL-240 data logger with a sample frequency of 0.1Hz was used for collecting TRFS and thermocouples data. The solar radiation intensity obtained by TRFS was also verified using RS Pro IM-750 solar power meter. To capture the thermal images on concretes surfaces FLIR T1050sc infrared camera was used. The camera has sensitivity less than 20mK and field of view 45º x 34º.

As shown in Figure 3, Concrete slabs were positioned upright, facing global N-S direction. A wooden structure made of two 25mm thick wooden sheets infilled with polystyrene boards was used to shield the slabs from direct solar irradiance. For Case-B, the north face of slabs was exposed to direct sunlight throughout the day. The infrared camera was setup on south face of the concrete slabs at 2m distance, and perpendicular to the surface. A customized wooden box shelter was made for infrared camera to protect it from weather conditions. The solar radiation intensity (W/m^2) on slab surface was measured using TRFS and stored using GL240 with

sampling frequency of 0.1Hz. The local weather station captured ambient temperature, humidity, and wind speed at every 10 minutes interval. Thermal images were also taken every 10 minutes with image resolution of 1024 x 768 pixels. FLIR Research IR software was used for post procession and data extraction of thermal images. Data for 7 consecutive days was collected for each study case.

2.3 Numerical Modelling

2.3.1 Governing equations

The heat transfer within a concrete lab can be expressed by well-known Fourier's heat flow equation[43]. That is,

$$\rho c \frac{\partial T}{\partial t} = k_x \frac{\partial^2 T}{\partial x^2} + k_x \frac{\partial^2 T}{\partial y^2} + k_x \frac{\partial^2 T}{\partial z^2} \quad (1)$$

where ρ and c are density (kg/m^3) and heat capacity (J/kg. K) of the concrete, respectively. k is the thermal conductivity corresponding to the respective axis (W/m. K), T is the absolute temperature (K), and t is time. The right-hand side of Equation *(1)* defines the rate of heat exchange at the boundary surface of slab. The heat exchange between the surrounding environment and slab surfaces is depicted in Figure 1.

2.3.2 Boundary equations

As the boundary heat loss or gain includes heat transfer through solar irradiation (q_s), radiation (q_r) and convection (q_c), the total boundary heat gain or loss q (W/m^2) is given by,

$$q = q_s + q_r + q_c \quad (2)$$

Heat exchange due to solar radiation in short wavelength is given by,

$$q_s = \alpha G \quad (3)$$

where α is solar absorptivity for concrete surface varying between 0.5-0.7[44]. G is solar irradiation at any instance of time. For surfaces with no direct solar radiation or under shade, $G=0$ and thereby $q_s = 0$

The boundary heat exchange due to long-range radiation q_r and convective q_c between concrete surface and surrounding depends upon the corresponding temperature differences. That is,

$$q_r = e\sigma(T^4 - T_0{}^4) \quad (4)$$

where T is the surface temperature of concrete at any time and T_0 is surrounding temperature. e is emissivity of material and σ represents the Stiffen Boltzmann constant.

$$q_c = h_c(T - T_0) \quad (5)$$

where h_c is the convection heat transfer coefficient (W/m^2. ^{o}C). Based on the study of Branco et. al [45], h_c for bridge structures exposed to wind flow can be defined as,

$$h_c = 6.0 + 3.7V \quad (6)$$

where V is wind velocity in m/s.

Numerical solutions

To model the heat transfer within the concrete, heat transfer module of commercial finite element software COMSOL Multiphysics[46] was implemented to solve the governing equations. The concrete slabs and internal defects were modelled using 3D solid elements. Free tetrahedral elements were used with mesh size range from 0.0075-0.6m, maximum element growth rate of 1.45 and curvature factor of 0.5. Table 3 shows the material properties used in this study[29]. The environmental factors such as solar radiation, ambient temperature, were treated as boundary conditions in this study. The ambient weather conditions during experiments (Case-A and Case-B) are shown in Figures 4 and 5.

The effects of the wind velocity and humidity were incorporated as bulk convection heat transfer coefficient (W/m^2. K) of the slabs. Hiasa et. al[39] has performed sensitivity analysis using numerical modelling for wind data with maximum speed of 3.3 m/s and proposed a bulk heat transfer coefficient of 20 W/m^2.K for slab samples under natural environmental condition. Similarly, Rumbayan[47], used a bulk heat transfer coefficient of 20 W/m^2.K in their study, while Wang et. al[48] performed experimental study on thermal behaviour of concrete box girder arch bridges and recommended that the heat transfer coefficients for top, bottom and internal surface of the girder 19.0 W/m^2. K, 12.5 W/m^2. K and 9.5 W/m^2. K, respectively. Considering the maximum wind velocity measured in this study, the bulk coefficient (h_c) of 19.0 W/m^2. K and 12.0 W/m^2. K were used for the surface and bottom of the slab, respectively.

3 RESULTS AND DISCUSSIONS

3.1 The experimental results

Figure 6 shows the typical thermal images by IR camera during the experimental study. A temperature contrast between delaminated subsurface and rest of the surface of concrete slabs can be seen in the thermogram. To quantitatively evaluate the information on the contrast in thermogram, the apparent temperature difference (absolute thermal contrast) between the defect and intact area was measured. The absolute thermal contrast (ΔT) was determined as,

$$\Delta T(t) = T_d(t) - T_s(t) \qquad (7)$$

where T_d is an average temperature for a 3x3 pixels matrix located on delaminated subsurface and T_s from sound surface. The time-dependent absolute thermal contrast was obtained for each defect region under different environmental conditions.

Figure 7 shows a week-long time-dependent ΔT for Cases A and Case B under different environmental conditions. The results in Figure 7a (Case A) show that the critical environmental parameter, which governs the thermal contrast development, is daily ambient temperature variation. The ΔT develops through convection heat exchange between slabs and surrounding environment. The time-dependent ΔT varied following a similar pattern of the daily temperature. During the daytime, as the ambient temperature rises, the heat transfers from surrounding environment into the concrete slabs. As the embedded delamination disrupts the heat flow through concrete, the temperature above the delamination rises relatively quickly as compared to the surrounding sound area. Therefore, a positive contrast is achieved according to Equation (7). Due to the high thermal mass, concrete absorbs and stores heat energy under

high temperature in daytime. When the ambient temperature starts dropping after midday and onward, the concrete radiates heat to the surrounding environment. Due to the thin section over the delamination, the heat radiates relatively quickly as compared to surrounding sound area, and therefore the thermal contrast becomes negative at night-time. The magnitude of ΔT attained was found to be dependent upon the daily variation of the ambient temperature.

For a relatively high daily temperature difference, the developed ΔT is high. As shown in Figure 7a, the daily variation for 22-June 2019 was recorded as 7.3ºC and the maximum ΔT for delamination *D1* during daytime was 0.1ºC, whereas, on 25-June 2019, the daily variation was recorded 14.7ºC and the maximum ΔT achieved for *D1* was 0.4ºC. Further, ΔT decreases with the increase of delamination depth. For example, in Figure 7a, ΔT for D3 is significantly higher than that of D2.

Figure 7b shows experimental results of Case-B, where the target surface is exposed to indirect solar radiation effect. As depicted in Figure 1 the heat exchange in this case takes place through both convection and radiation. During daytime the slab surfaces on both sides heat up due to convection heat exchange with the surrounding environment which is same as that of Case A. Additionally, as the back surface is exposed to direct sunlight, the heat exchange through irradiation also takes place. The heat then travels to the other side of slab through conduction from within the slab. It is observed that the dominant environmental factor in this case is the solar radiation on the back of slab. As shown in Figure 7b, unlike Case A, there is very little, or no positive thermal contrast observed during the experimental program. The measured thermal contrast for all three defects remains negative most of the time, particularly during daytime. The positive contrast appears for a very short period, and that happens during late night or early morning times. The development of negative contrast during daytime is an indication that more heat is transferred through conduction from the back of slab to the front surface. If there is an internal defect, the surface temperature above defected region is lower than that in the surrounding environment. In addition, the size of delamination also plays an important role in ΔT. For relatively large delamination (D1), the increase in contrast ΔT is faster than that of a relatively small (D2). However, the peak of ΔT of both cases reached at the same time shortly after the sunset. Furthermore, it shows that ΔT is also influenced by other environmental parameters (*e.g.* wind velocity) besides ambient temperature variation. Considering the weather data in Figure 4, it is observed that a sudden increase in wind velocity also affects the ambient temperature variation.

3.2 Numerical model validation

In this section, the developed numerical model was validated using experimental results. Figures 8 and 9 show the comparison between the numerical predictions and the experimental data. The numerical model predicted thermal contrasts are plotted along with the experimental results for each of the defect in separate figures. The results demonstrate that the developed model can describe the experimentally measured thermal contracts of all three types of defects reasonably well, for both cases (Case-A and Case-B).

3.3 Parametric studies

After validation, the developed model was implemented to investigate the effects of various environmental parameters on thermal contracts of different defect characteristics with/without direct solar radiation. The model parameters considered in this study are as follows:

- Daily variation of ambient temperature
- Diurnal solar radiation flux throughout the year
- Thickness of bridge deck slab
- Depth of delamination
- Area of delamination

The values of parameters used in this parametric study are shown in Table 4. The solar radiation of a day randomly selected from March, June, September, and December of Australia was used in numerical modelling. For daily ambient temperature variation, it is assumed that ambient temperature follows a sinusoidal curve between maximum and minimum daily temperature[49, 50]. The minimum temperature is assumed to occur at 3:00 hr during night and maximum temperature around 15:00hr in the day. Considering these approximations, the daily variation of ambient temperature used in the model is given by,

$$T_a(t) = T_{avg} + delT \times \cos \pi\left(\frac{t-15}{12}\right) \quad (8)$$

where T_a is ambient temperature at any time of the day, T_{avg} is the average of maximum and minimum daily temperature, and $delT$ is half daily variation. The effect of wind velocity was indirectly modelled using bulk convection heat transfer coefficient.

The purpose of this parametric study is to identify the optimal environmental condition that could lead to detectable thermal contrast under indirect/no solar radiation condition. ASTM D4788-03[37] recommends a minimum thermal contrast of 0.5ºC for successful application of IRT techniques.

Ambient temperature variation (Case A.1): Figure 10a shows the effects of daily variation of ambient temperature on the thermal contrast development on concrete surface. It shows that ΔT follows the same trend as the ambient temperature. The peak thermal contrast happens at noon time and midnight. The thermal contrast increases with the increase of the daily variation in ambient temperature (*delT*). It shows that the ΔT primarily depends upon the daily variation of temperature *(delT),* regardless of the daily maximum or minimum temperature. For example, in Figure 10a, under the same daily variation *(delT=5)*, the two curves overlap although the average daily temperature for one curve is 5ºC and the other is 12ºC. Figure 10b presents the maximum thermal contrast attained for different daily variation of temperature. It demonstrates a linear relationship between the thermal contrast and the rate of change of daily temperature. For a 300cm^2 delamination, located at 3.0 cm from surface, minimum 6.0ºC change in ambient temperature in 12 hours (0.5ºC/hr) is required to generate a 0.5 ºC of thermal contrast.

Solar radiation intensity (Case B.1): Figure 11 shows the thermal contrast development on concrete surface due to indirect solar radiation impact (*i.e.,* radiation at back). It shows the time dependent thermal contrast under diurnal variation of solar intensities for four different periods

of the year. It can be seen that the thermal contrast increases with the increase of the radiation intensities. Interestingly, there is little positive thermal contrast development when the back surface of slab is exposed to direct radiation. Initially, due to convection heat transfer between slab surface and ambient temperature, a relatively small thermal contrast on positive side is developed. However, as the back of slab heats up due to radiation, the heat travels toward the front surface through conduction. As the influx of heat due to conduction overtakes the convection heat, the thermal contrast becomes negative (as depicted in Figure 1). The maximum thermal contrast appears after the sunset and keeps well below 0.5 ^{o}C throughout the night. A maximum diurnal radiation intensity of 600 W/m^2 for a clear day is good enough to develop a detectable thermal contrast for a 300cm^2 at a depth of 3.0cm from surface, at nighttime.

Thickness of bridge deck (Case A.2 and B.2): Figure 12 shows the time dependent ΔT for two different slab thicknesses of bridge deck. It reveals that the slab thickness has a significant impact on thermal contrast development, *i.e.* the thermal contrast increases with the increase in the thickness of slab. Because, heating up a thick concrete slab requires more energy and takes longer time whereas, the concrete thickness over the delamination remains the same. Similarly, as the thick slab can store more energy during daytime, therefore it takes longer than thin section, to radiate the heat and cool down in night-time. Hence, for thicker section the developed negative thermal contrast is higher as well, according to equation 7.

For the slab without solar radiation exposure, the thermal contrast changes following the pattern of ambient temperature and reaches to its peaks in afternoon and midnight time, respectively. Due to more thermal mass, the positive and negative thermal contrast peaks for thick slabs appears later than the thin sections and the magnitude is also high. For the slabs with solar radiation on back (indirect radiation), initially a positive thermal contrast appears for a short period due to convection heat transfer. However, soon after the sunrise, the heat transfers from the back surface towards the front surface of the slab through conduction. Same as the slabs without solar radiation, the developed thermal contrast for thick slab sections has higher magnitude and appears later than thin section. Table 5 summarizes the peak negative and positive thermal contrast with different slab thicknesses with and without solar radiation, respectively. In both cases, the maximum positive and negative thermal contrasts increase with the increase of the slab thickness.

Depth of delamination (Case A.3 and B.3): Figure 13 shows the time dependent variation of absolute thermal contrast for two different depths of delamination for both Case A and Case B, respectively. The Table 6 summarizes the simulation results. It shows that the thermal contrast decreases with the increase of the delamination depth for both cases. There is a linear relationship between ΔT and square of delamination depth. For a deep delamination (i.e., 5.0cm), the contrast over the threshold of 0.5 ^{o}C appears for a very short period. In addition, the depth of delamination has very little impact on the time required to reach the maximum thermal contrast (i.e., the peaks appear at similar time window of the day/night).

Area of delamination (Case A.4 and B.4): Figure 14 shows the time-dependent thermal contrast of different sizes of delamination and Table 7 summarizes the simulation outcomes. It indicates that the ΔT initially increases with the increase of delamination size. However, for a

relatively large delaminations (i.e. >300cm^2), the difference in ΔT is not significant. The delamination size also has no impact on time window of the day/night at which the maximum thermal contrast appears.

4 CONCLUSIONS

The purpose of this study is to expand the application of IRT for delamination detection of bridge sections which are not exposed to direct solar radiation. Both experimental and numerical studies were carried out to investigate the effects of a range of factors (e.g. environmental variables, thickness of bridge deck and defect characteristics) on the absolute thermal contrast (ΔT) development. The following are some major conclusions:

- The infrared thermography can be effectively applied to detect the subsurface delamination of concrete bridge deck which is not exposed to the direct solar radiation.
- The developed numerical model can predict the effects of environmental parameters, thickness of bridge deck and characteristics of delamination on the ΔT development. The model predictions match the experimental results reasonably well.
- In case of no radiation (Case-A), the thermal contrast development depends upon the rate of change in ambient temperature. For the case of indirect solar radiation (Case-B), the radiation on back surface of the slab has greater impact on contrast development than that of the daily variation of ambient temperature.
- For Case-A, a rate of change in ambient temperature of 0.5^{o}C/hr could produce a detectable contrast ΔT (>0.5^{o}C) for a 300cm^2 delamination at depth of 3.0cm from the surface. However, the contrast can only last a very short period of time. Considering the duration of thermal contrast and other factors, such as environmental variables, at least 1^{o}C/hr is recommended for effective utilization of IRT.
- For Case-B, a clear day noon radiation intensity > 600 W/m^2 is recommended to produce a detectable thermal contrast by IRT.
- For Case A, the suitable time for IRT inspection is around noon time and midnight. For Case-B, the suitable time for IRT is from sunset to sunrise, preferably midnight when the ΔT is expected to be the highest.
- For Case-A, the thickness of deck slab has significant impact on the thermal contrast development as well as the time window to achieve the peak thermal contrast. ΔT increases with the increase of the thickness of deck slab. However, for Case-B, the impact of the thickness of the slab on the maximum ΔT is limited. For Case-A, the detectable ΔT happens during the period between 8:00 to16:00, while for Case-B, the best time for IRT inspection is between 18:00 to 4:00.
- ΔT decreases with the increase of the depth of delamination, while ΔT increases with the increase of the delamination size. However, depth and size have very little impact on the time window to achieve maximum thermal contrast.

It should be mentioned that the application of IRT in detecting delamination in a concrete deck could be rather challenging under a complex surrounding environment, such as having a concrete deck with a mixed shaded/non-shaded pattern. Although our previous study has investigated the intermittent shading effect (e.g., transient cloud cover)[29], further experimental

work is required in order to fundamentally understand how to implement IRT in delamination detection of a bridge concrete deck in an effective way under different complex surrounding environmental conditions. In addition, our future study will focus on the investigation of the implementation of UAVs in IRT inspection with the aim of detecting the delamination in concrete deck both efficiently and effectively.

5 ACKNOWLEDGEMENTS

The authors wish to thank the Australian Research Council (ARC IH150100006) and CRC Bushfire & Natural Hazards. The authors would also like to thank Higher Education Commission Pakistan (HRDI—Faculty Development of UESTPs-UETs Phase-1) and The University of Melbourne for their support.

6 REFERENCES

1. Koh CG, Ang KK, Zhang L. Effects of repeated loading on creep deflection of reinforced concrete beams. *Engineering Structures.* 1997;19:2--18.

2. Tran QH, Han D, Kang C, Haldar A, Huh J. Effects of Ambient Temperature and Relative Humidity on Subsurface Defect Detection in Concrete Structures by Active Thermal Imaging. *Sensors.* Aug 2017;17(8).

3. Maizuar M, Zhang L, Miramini S, Mendis P, Thompson RG. Detecting structural damage to bridge girders using radar interferometry and computational modelling. *Structural Control & Health Monitoring.* 2017;24(UNSP e1985).

4. Sun D, Wu K, Miramini S, Zhang L. Deformation behaviour of concrete materials under the sulfate attack. *Construction and Building Materials.* 2019;210:232-241.

5. Sun D, Wu K, Shi H, Zhang L, Zhang L. Effect of interfacial transition zone on the transport of sulfate ions in concrete. *Construction and Building Materials.* 2018;192:28--37.

6. Sun D, Shi H, Wu K, Miramini S, Li B, Zhang L. Influence of aggregate surface treatment on corrosion resistance of cement composite under chloride attack. *Construction and Building Materials.* 2020;248:118636.

7. Russell HG. *Concrete bridge deck performance.* Vol 333: Transportation Research Board; 2004.

8. Su RKL, Zhang Y. A double-cylinder model incorporating confinement effects for the analysis of corrosion-caused cover cracking in reinforced concrete structures. *Corrosion Science.* 2015;99:205-218.

9. Washer G, Bolleni N, Fenwick R. Thermographic imaging of subsurface deterioration in concrete bridges. *Transportation research record.* 2010;2201(1):27-33.

10. Clark MR, McCann DM, Forde MC. Application of infrared thermography to the non-destructive testing of concrete and masonry bridges. *Ndt & E International.* Jun 2003;36(4):265-275.

11. Washer G, Fenwick R, Nelson S, Rumbayan R. Guidelines for thermographic inspection of concrete bridge components in shaded conditions. *Transportation research record.* 2013;2360(1):13-20.

12. Mac VH, Huh J, Doan NS, Shin G, Lee BY. Thermography-Based Deterioration Detection in Concrete Bridge Girders Strengthened with Carbon Fiber-Reinforced Polymer. *Sensors.* 2020;20(11):3263.

13. Hiasa S, Karaaslan E, Catbas FN. *Considerations for Infrared Thermography Field Implementations and Data Analysis for Bridge Inspections* 2018.

14. Kazmi SMS, Munir MJ, Wu Y-F, Patnaikuni I. Effect of macro-synthetic fibers on the fracture energy and mechanical behavior of recycled aggregate concrete. *Construction and Building Materials.* 2018;189:857-868.

15. Munir MJ, Wu Y-F, Kazmi SMS, Patnaikuni I, Zhou Y, Xing F. Stress-strain behavior of spirally confined recycled aggregate concrete: An approach towards sustainable design. *Resources, Conservation and Recycling.* 2019;146:127-139.

16. Li C-Q, Yang S. Prediction of concrete crack width under combined reinforcement corrosion and applied load. *Journal of engineering mechanics.* 2011;137(11):722-731.

17. Gucunski N, Council NR. *Nondestructive testing to identify concrete bridge deck deterioration*: Transportation Research Board; 2013.

18. Rehman SKU, Ibrahim Z, Memon SA, Jameel M. Nondestructive test methods for concrete bridges: A review. *Construction and building materials.* 2016;107:58-86.

19. Oh T, Kee S-H, Arndt RW, Popovics JS, Zhu J. Comparison of NDT methods for assessment of a concrete bridge deck. *Journal of Engineering Mechanics.* 2013;139(3):305-314.

20. Sack DA, Olson LD. Advanced NDT methods for evaluating concrete bridges and other structures. *NDT & e International.* 1995;28(6):349-357.

21. Rathod H, Gupta R. Sub-surface simulated damage detection using Non-Destructive Testing Techniques in reinforced-concrete slabs. *Construction and Building Materials.* 2019;215:754-764.

22. Yehia S, Abudayyeh O, Nabulsi S, Abdelqader I. Detection of common defects in concrete bridge decks using nondestructive evaluation techniques. *Journal of Bridge Engineering.* 2007;12(2):215-225.

23. Vaghefi K, Melo e Silva H, Harris D, Ahlborn R. Application of thermal IR imagery for concrete bridge inspection. Paper presented at: PCI National Bridge Conference, PCI/NBC, Salt Lake City: UT (USA), 2011.

24. Sony S, Laventure S, Sadhu A. A literature review of next-generation smart sensing technology in structural health monitoring. *Structural Control and Health Monitoring.* 2019;26(3):e2321.

25. Dorafshan S, Thomas RJ, Maguire M. Fatigue crack detection using unmanned aerial systems in fracture critical inspection of steel bridges. *Journal of bridge engineering.* 2018;23(10):04018078.

26. Rakha T, Gorodetsky A. Review of Unmanned Aerial System (UAS) applications in the built environment: Towards automated building inspection procedures using drones. *Automation in Construction.* 2018;93:252-264.

27. Kim I-H, Jeon H, Baek S-C, Hong W-H, Jung H-J. Application of crack identification techniques for an aging concrete bridge inspection using an unmanned aerial vehicle. *Sensors.* 2018;18(6):1881.

28. Omar T, Nehdi ML. Remote sensing of concrete bridge decks using unmanned aerial vehicle infrared thermography. *Automation in Construction.* 2017;83:360-371.

29. Raja BNK, Miramini S, Duffield C, Sofi M, Mendis P, Zhang L. The influence of ambient environmental conditions in detecting bridge concrete deck delamination using infrared thermography (IRT). *Structural Control and Health Monitoring.* 2020;27(4):e2506.

30. Hiasa S, Birgul R, Matsumoto M, Catbas FN. Experimental and numerical studies for suitable infrared thermography implementation on concrete bridge decks. *Measurement.* 2018;121:144-159.

31. Dabous SA, Yaghi S, Alkass S, Moselhi O. Concrete bridge deck condition assessment using IR Thermography and Ground Penetrating Radar technologies. *Automation in Construction.* 2017;81:340-354.

32. Cheng C, Na R, Shen Z. Thermographic Laplacian-pyramid filtering to enhance delamination detection in concrete structure. *Infrared Physics & Technology.* 2019;97:162-176.

33. Milovanović B, Gaši M, Gumbarević S. Principal Component Thermography for Defect Detection in Concrete. *Sensors.* 2020;20(14):3891.

34. Omar T, Nehdi ML, Zayed T. Infrared thermography model for automated detection of delamination in RC bridge decks. *Construction and Building Materials.* 2018;168:313-327.

35. Khan F, Rajaram S, Vanniamparambil PA, et al. Multi-sensing NDT for damage assessment of concrete masonry walls. *Structural Control and Health Monitoring.* 2015;22(3):449-462.

36. Washer G, Fenwick R, Bolleni N, Alampalli S. Development of hand-held thermographic inspection technologies. *Materials Evaluation.* 2008;66(3).

37. Standard A. D4788-03 (2013).“Standard Test Method for Detecting Delaminations in Bridge Decks Using Infrared Thermography.”. *ASTM International.*

38. Rocha JHA, Póvoas YV, Santos CF. Detection of delaminations in sunlight-unexposed concrete elements of bridges using infrared thermography. *Journal of Nondestructive Evaluation.* 2019;38(1):8.

39. Hiasa S, Birgul R, Catbas FN. Investigation of effective utilization of infrared thermography (IRT) through advanced finite element modeling. *Construction and Building Materials.* 2017;150:295-309.

40. Washer G, Fenwick R, Bolleni N. Effects of solar loading on infrared imaging of subsurface features in concrete. *Journal of Bridge Engineering.* 2010;15(4):384-390.

41. Watase A, Birgul R, Hiasa S, Matsumoto M, Mitani K, Catbas FN. Practical identification of favorable time windows for infrared thermography for concrete bridge evaluation. *Construction and Building Materials.* 2015;101:1016-1030.

42. Kee S-H, Oh T, Popovics JS, Arndt RW, Zhu J. Nondestructive bridge deck testing with air-coupled impact-echo and infrared thermography. *Journal of Bridge Engineering.* 2012;17(6):928-939.

43. Abid SR, Mussa F, Tayşi N, Özakça M. Experimental and finite element investigation of temperature distributions in concrete-encased steel girders. *Structural Control and Health Monitoring.* 2018;25(1):e2042.

44. Larsson O, Thelandersson S. Estimating extreme values of thermal gradients in concrete structures. *Materials and structures.* 2011;44(8):1491-1500.
45. Branco FA, Mendes PA. Thermal actions for concrete bridge design. *Journal of Structural Engineering.* 1993;119(8):2313-2331.
46. Comsol A. Heat transfer module. *User's guide.* 2019.
47. Rumbayan R. *Modeling of environmental effects on thermal detection of subsurface damage for concrete bridges*, University of Missouri--Columbia; 2013.
48. Wang Y, Zhan Y, Zhao R. Analysis of thermal behavior on concrete box-girder arch bridges under convection and solar radiation. *Advances in Structural Engineering.* 2016;19(7):1043-1059.
49. Elbadry MM, Ghali A. Temperature variations in concrete bridges. *Journal of Structural Engineering.* 1983;109(10):2355-2374.
50. Dilger WH, Ghali A, Chan M, Cheung MS, Maes MA. Temperature stresses in composite box girder bridges. *Journal of Structural Engineering.* 1983;109(6):1460-1478.

FIGURES AND TABLES

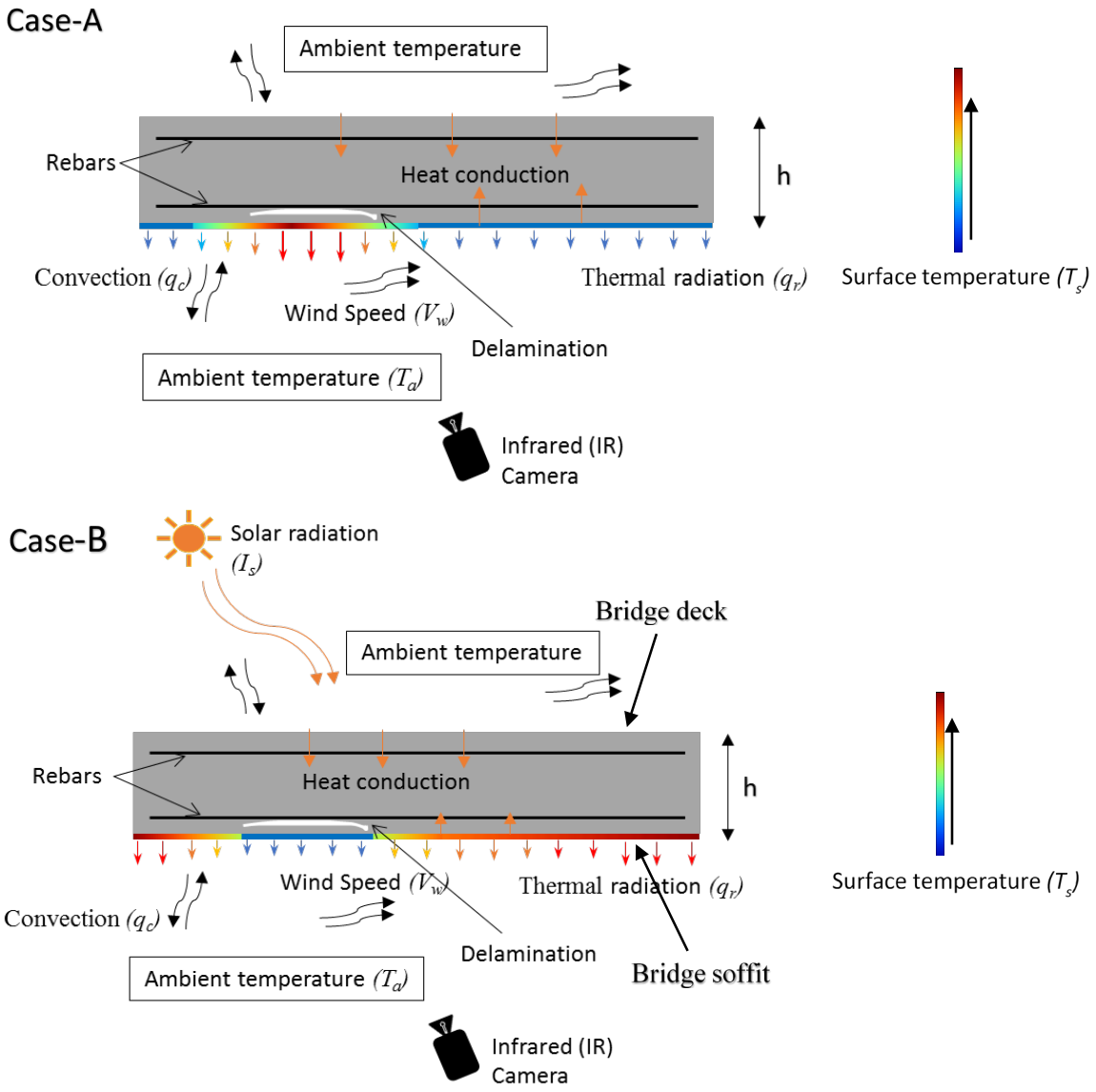

Figure 1: Thermal response of subsurface defects in bottom concrete bridge deck, and thermal exchange between concrete and surrounding environment (Case-A) Not exposed to the solar radiations; (Case-B) Exposed to indirect solar radiations impacts.

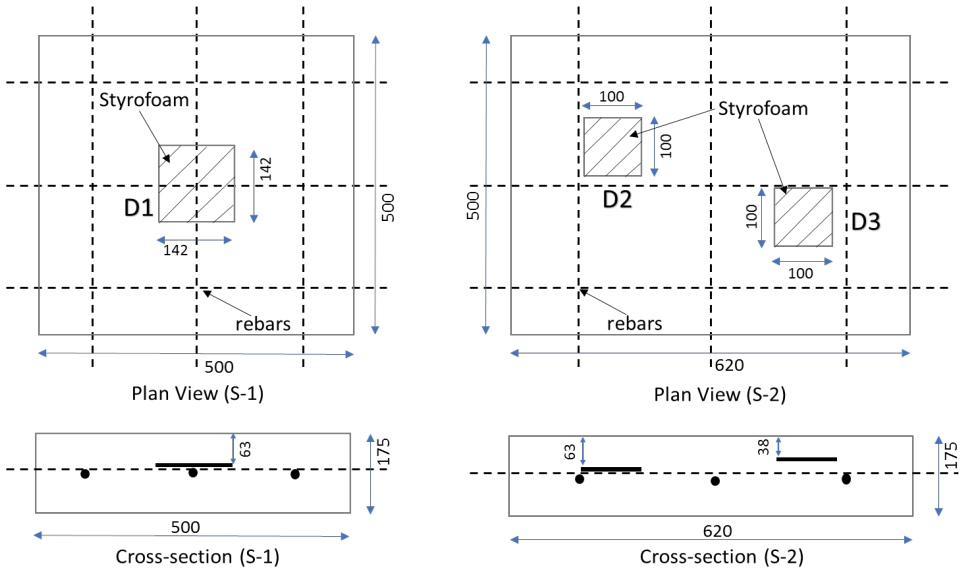

(a)

(b)

Figure 2 : Construction of concrete slab samples used in this study *(a)* Details of the slab sample design; and *(b)* Casting of concrete slab samples

Table 1: Details of slab sample design

Slab details		**Delamination details**			
Description	Size (mm^3)	Description	Size (mm × mm)	Thickness (mm)	Depth from surface, *d* (mm)
S - 1	500 × 500 × 175	D1	141.5 × 141.5	5	63
S – 2	500 × 620 × 175	D2	100 × 100	5	63
		D3	100 × 100	5	38

Table 2. Concrete mix details

Description	Details
Cement: Sand: Coarse aggregates	1:2:2
Maximum aggregate size	10 mm
Water cement ratio	0.6

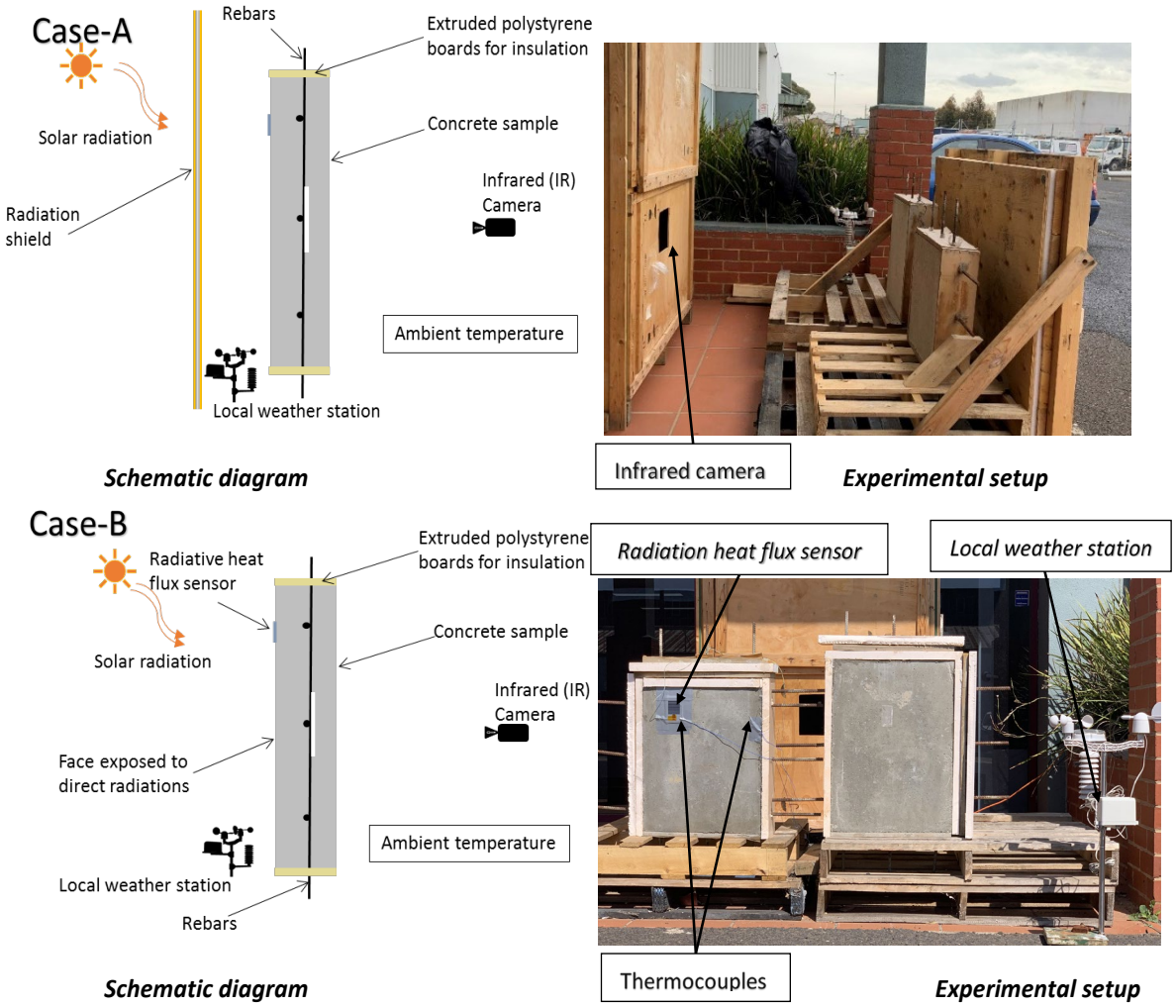

Figure 3: Details of experimental setup. Case-A: not exposed to direct solar radiation; and Case-B: exposed to indirect solar radiation

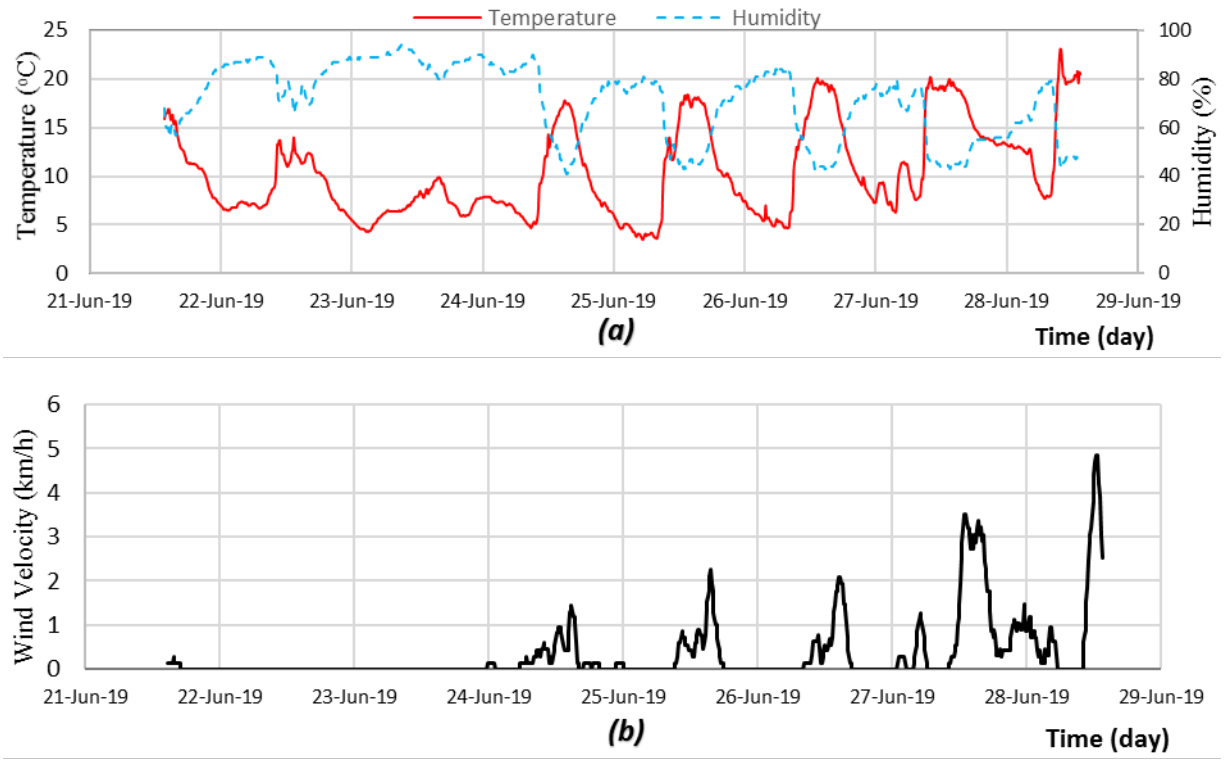

Figure 4: Ambient weather data collected during the experimental period (Case A), *(a)* Ambient temperature and Humidity; and *(b)* Wind velocity

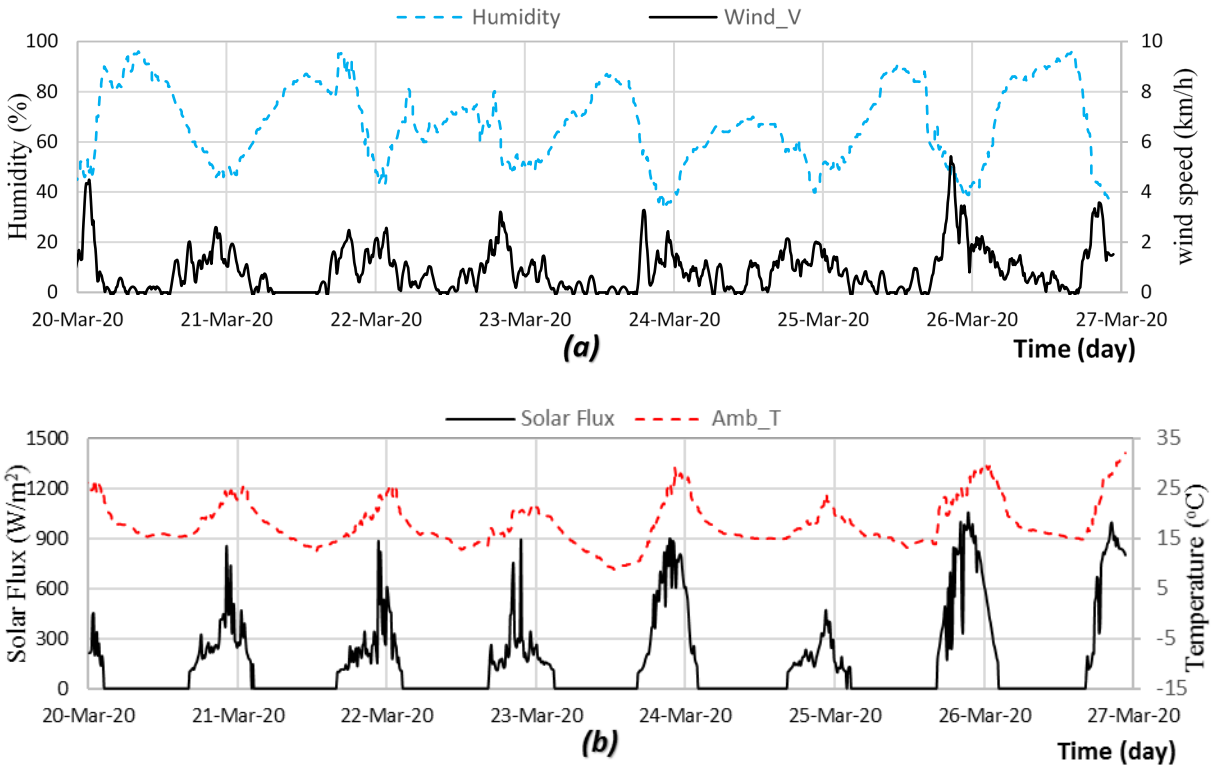

Figure 5: The ambient weather data collected during the experimental period (Case B), *(a)* Humidity and wind speed; and *(b)* Ambient temperature and radiation heat flux on surface

Table 3. Details of the material properties used in numerical modelling

Material properties	**Concrete**	**Styrofoam**
Thermal conductivity (W/m. K)	1.7	0.024
Specific heat (J/kg. K)	900	1130
Density (kg/m^3)	2300	25
Solar absorption coefficient, α	0.70	-
Surface emissivity, *e*	0.92	-

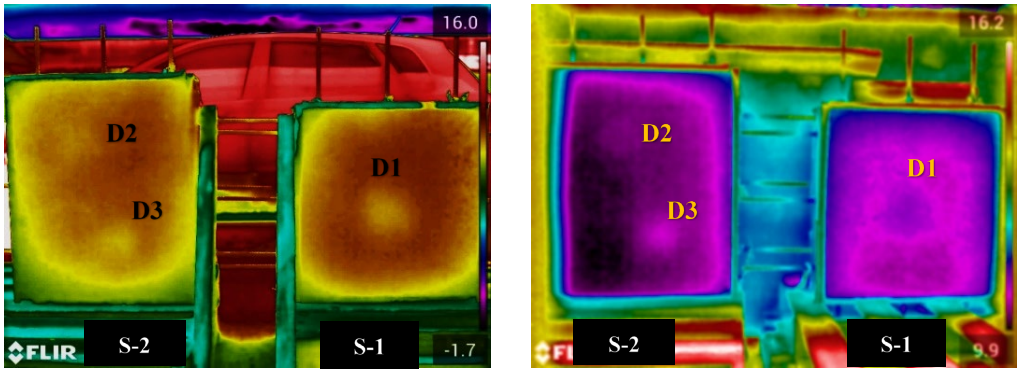

Figure 6: The typical thermal images (thermogram) of Case-A and Case-B, respectively

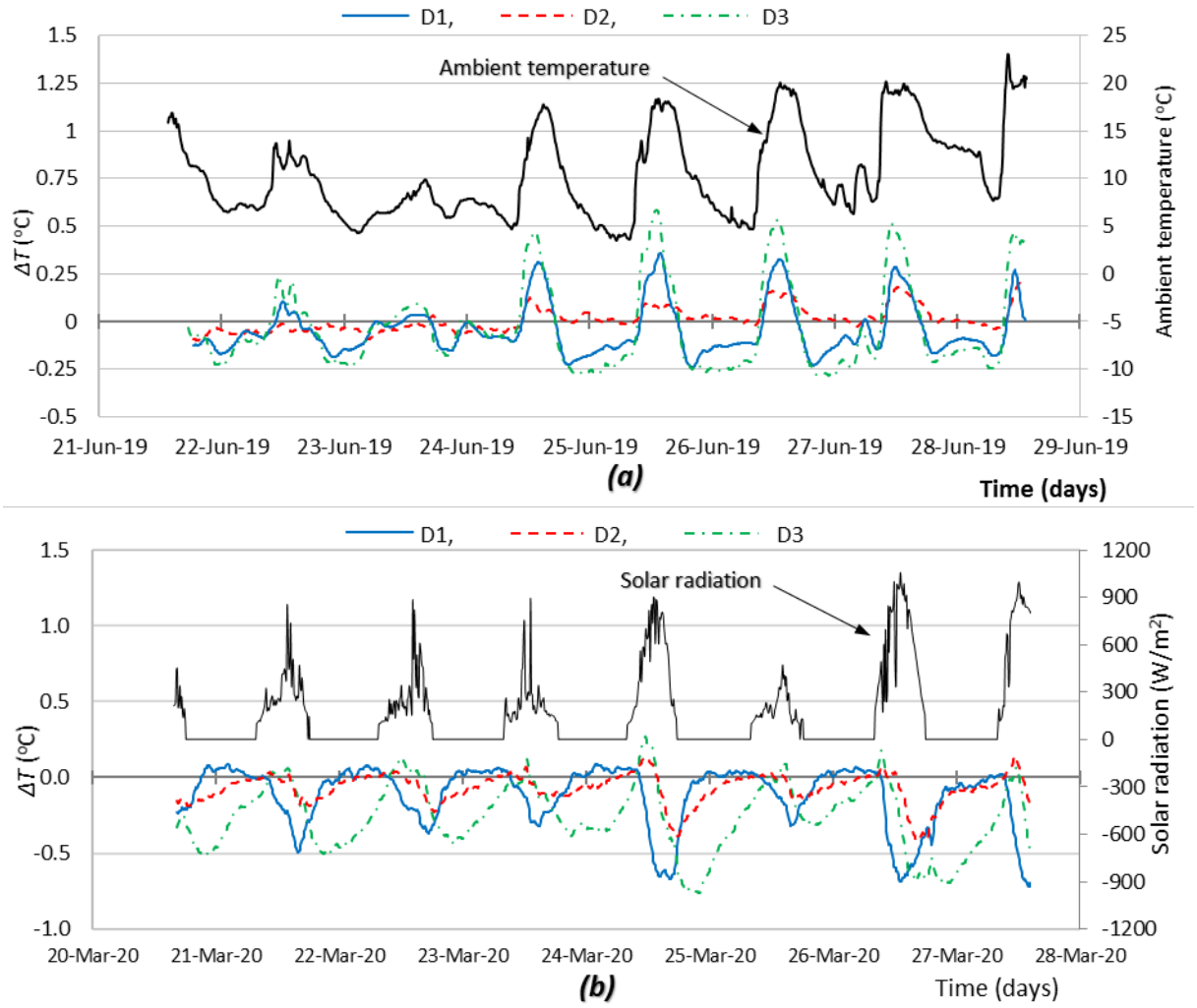

Figure 7: Time dependent thermal contrast of test slabs under different environmental conditions. *(a)* without solar radiation (Case-A) and *(b)* with solar radiation (Case-B)

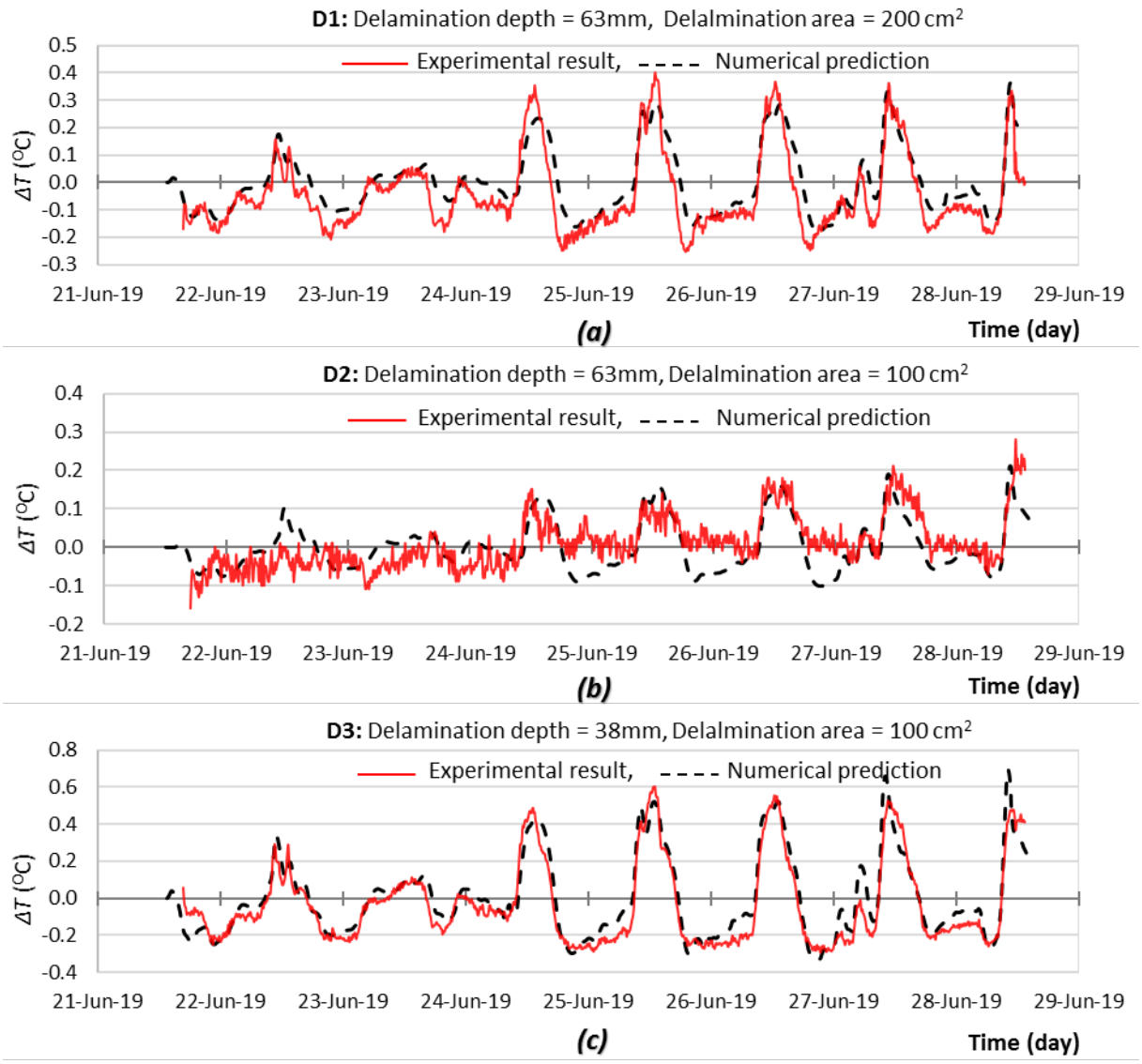

Figure 8: Comparison between numerical model prediction and experimentally measured thermal contrast (Case-A), *(a)* D1: delamination depth = 63mm, delamination area = 200cm^2, *(b)* D2: delamination depth = 63mm, delamination area = 100cm^2 and *(c)* D3: delamination depth = 38mm, delamination area = 100cm^2

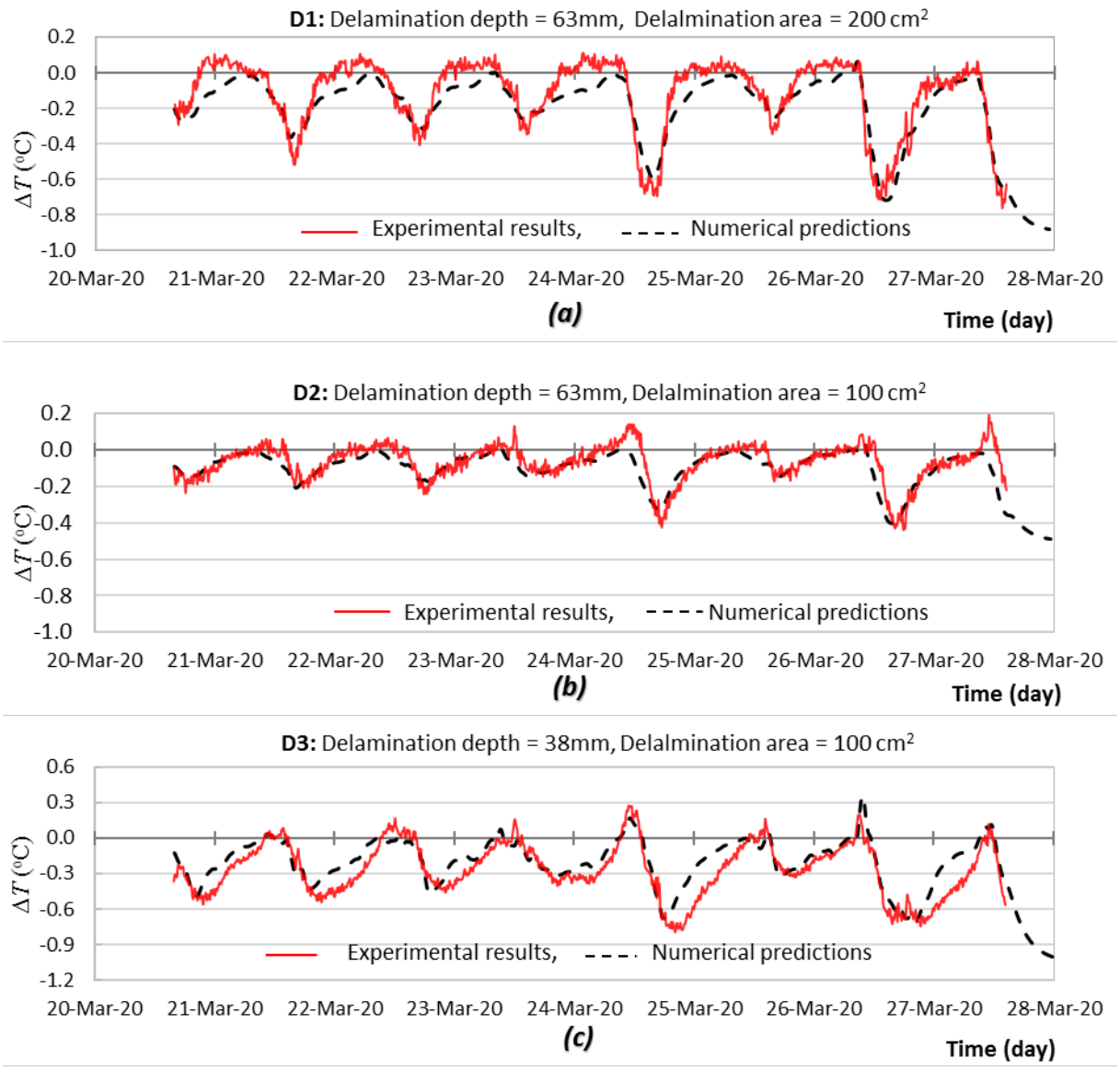

Figure 9: Comparison between numerical model prediction and experimentally measured thermal contrast (Case-B), (a) D1: delamination depth = 63mm, delamination area = 200cm^2, (b) D2: delamination depth = 63mm, delamination area= 100cm^2 and (c) D3: delamination depth = 38mm, delamination area = 100cm^2

Table 4: Values of parameters used in the parametric study

Parametric Studies					
Case	Ambient Temperature (°C)	Maximum solar radiation flux on		Delamination Depth (cm)	

		Average Daily ($T_{avg.}$)	Half daily Variation (*del T*)	concrete surface for a clear day at different periods of year (W/m^2)	Slab Thickness (cm)		Delamination Size (cm^2)
Case A	A.1	12	2.5 to 12.5	x	20	3.0	300
	A.2	12	7.5	x	17.5 to 35	3.0	300
	A.3	12	7.5	x	20	1.0 to 6.0	300
	A.4	12	7.5	x	20	3.0	100 to 350
Case B	B.1	12	7.5	1250 (Summer) 1020 (Fall) 625 (Winter) 1025 (Spring)	20	3.0	300
	B.2	12	7.5	1020	17.5 to 35	3.0	300
	B.3	12	7.5	1020	20	1.0 to 6.0	300
	B.4	12	7.5	1020	20	3.0	100 to 350

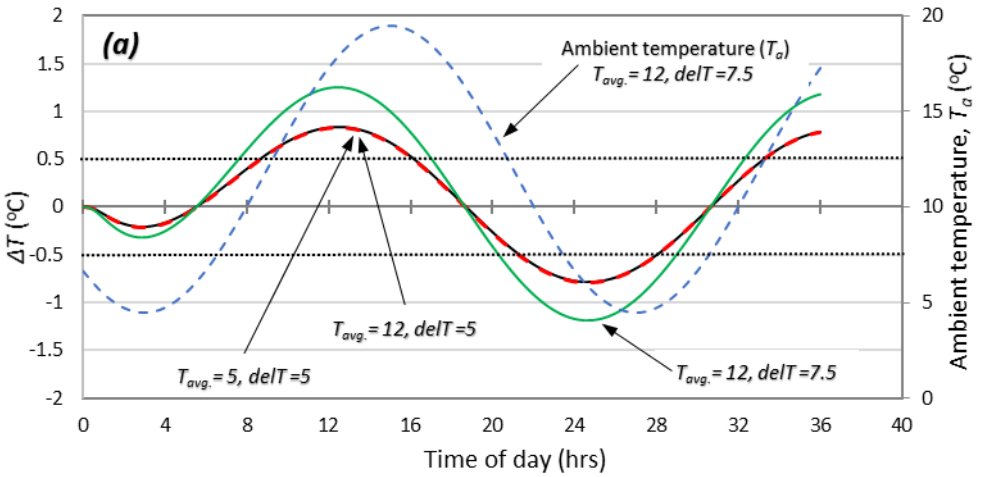

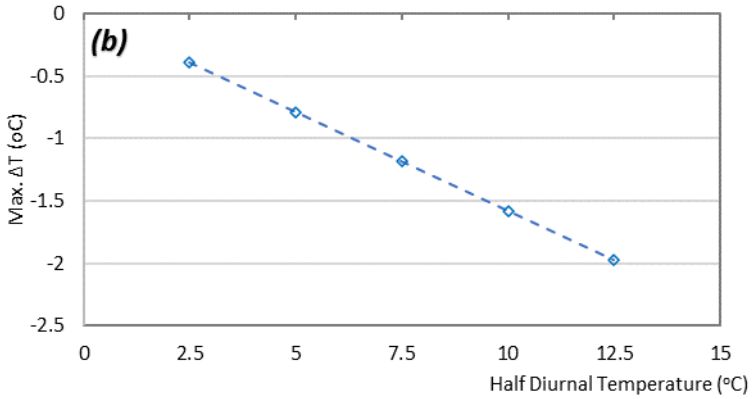

Figure 10: (a) Development of thermal contrast with ambient temperature variation and no solar radiation, (b)Maximum thermal contrast under different daily variation of temperature *(Delamination depth = 3.0 cm, area = 300 cm^2, thickness = 5.0 mm and slab thickness = 20 cm)*

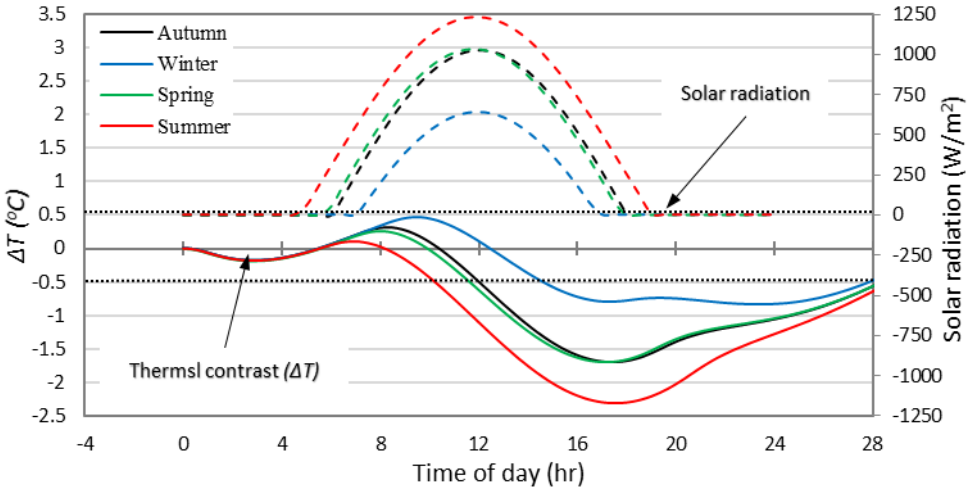

Figure 11: Time dependent variation in thermal contrast under diurnal solar radiation intensities for different periods of year *(Delamination depth = 3.0 cm, area = 300 cm^2, thickness = 5.0 mm and slab thickness = 20 cm)*

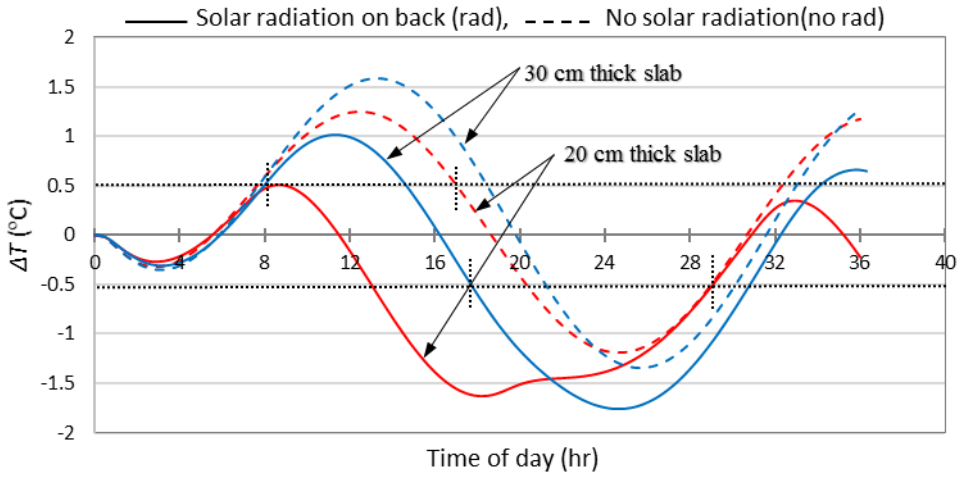

Figure 12: Time dependent thermal contrast for two different thickness of bridge deck with and without solar radiation *(delamination depth = 3.0 cm, area=300 cm^2 and thickness = 5 mm)*

Table 5: Maximum thermal contrast achieved for different thicknesses of slab

Thickness of Slab (cm)	**No solar radiation**		**Indirect solar radiation**	
	Positive ΔT Max. (°C)	Negative ΔT Max. (°C)	Positive ΔT Max. (°C)	Negative ΔT Max. (°C)
17.5	1.11	-1.09	0.23	-1.87
20	1.25	-1.19	0.27	-1.64
25	1.45	-1.31	0.48	-1.68
30	1.58	-1.34	0.63	-1.79
35	1.66	-1.32	0.78	-1.80

**delamination depth = 3.0 cm, area=300 cm^2 and thickness = 5 mm*

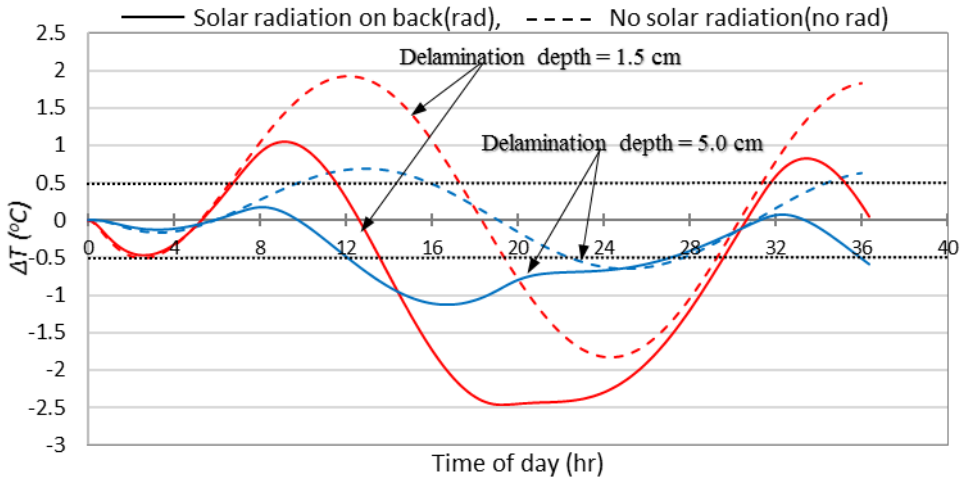

Figure 13: Time dependent thermal contrast for two different depths of delamination with and without solar radiation *(delamination area = 300 cm^2, thickness = 5 mm and Slab thickness = 20 cm)*

Table 6: Maximum thermal contrast achieved for different depths of delamination

Depth of Delamination (cm)	**No solar radiation**		**Indirect solar radiation**	
	Positive ΔT Max. (°C)	Negative ΔT Max. (°C)	Positive ΔT Max. (°C)	Negative ΔT Max. (°C)
1.0	2.10	-2.09	1.08	-2.88
1.5	1.82	-1.82	0.82	-2.46
3.0	1.18	-1.19	0.34	-1.63
5.0	0.63	-0.65	0.07	-1.13
6.0	0.45	-0.48	0.02	-1.01

**delamination area = 300 cm², thickness = 5 mm and Slab thickness = 20 cm*

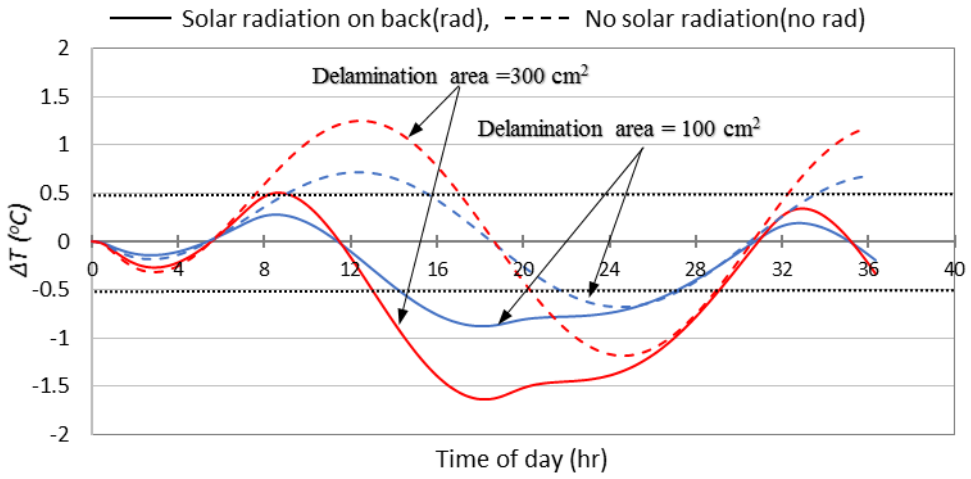

Figure 14: Time dependent thermal contrast for two different areas of delamination with and without solar radiation *(delamination depth = 3.0 cm, thickness = 5 mm and Slab thickness = 20 cm)*

Table 7: Maximum thermal contrast achieved for different areas of delamination

Area of Delamination (cm^2)	**No solar radiation**		**Indirect solar radiation**	
	Positive ΔT Max. (°C)	Negative ΔT Max. (°C)	Positive ΔT Max. (°C)	Negative ΔT Max. (°C)
100	0.7	-0.7	0.27	-0.88
200	1.0	-1.0	0.42	-1.35
300	1.2	-1.2	0.50	-1.64
350	1.3	-1.3	0.54	-1.74

**delamination depth = 3.0 cm, thickness = 5 mm and Slab thickness = 20 cm*